

PAPER

Multi-physics modeling of a spark plasma jet igniter

To cite this article: Xiaochi Ma *et al* 2022 *J. Phys. D: Appl. Phys.* **55** 035201

View the [article online](#) for updates and enhancements.

You may also like

- [Experimental study on energy characteristics and ignition performance of recessed multichannel plasma igniter](#)
Bang-Huang Cai, , Hui-Min Song et al.
- [Application study on plasma ignition in aeroengine strut-cavity-injector integrated afterburner](#)
Li FEI, , Bingbing ZHAO et al.
- [Evaluation of Oxygen Reduction System \(ORS\) in Large-scale Fire Tests](#)
Xiangyang Zhou, Yibing Xin and Sergey Dorofeev



The Electrochemical Society
Advancing solid state & electrochemical science & technology

241st ECS Meeting

May 29 – June 2, 2022 Vancouver • BC • Canada

Extended abstract submission deadline: Dec 17, 2021





Connect. Engage. Champion. Empower. Accelerate.
Move science forward



Submit your abstract



Multi-physics modeling of a spark plasma jet igniter

Xiaochi Ma¹ , Yifei Zhu^{1,2,*} , Yun Wu^{1,3,*} , Xiancong Chen³  and Bingxuan Lin⁴

¹ Institute of Aero-engine, School of Mechanical Engineering, Xi'an Jiaotong University, Xi'an 710049, People's Republic of China

² School of Electrical Engineering, Xi'an Jiaotong University, Xi'an 710049, People's Republic of China

³ Science and Technology of Plasma Dynamics Laboratory, Airforce Engineering University, Xi'an 710038, People's Republic of China

⁴ State Key Laboratory of Aerodynamics, China Aerodynamics Research and Development Center, Mianyang 621000, People's Republic of China

E-mail: yifei.zhu.plasma@gmail.com and wuyun1223@126.com

Received 11 July 2021, revised 23 September 2021

Accepted for publication 29 September 2021

Published 18 October 2021



Abstract

The plasma-fluid multi-physics process of a spark plasma jet igniter is studied numerically. The plasma discharge, gas heating, mass, and heat transfer processes in one working cycle are modeled and analyzed. Gas discharge starts inside the igniter, the 'ladder-like' dielectric wall structure promotes the transition of a volumetric discharge to a surface discharge, establishing a conductive path between the electrodes over a timescale of tens of nanoseconds. Once the electrodes are short-circuited, a new spark-arc discharge channel forms, heating the gas up to 7000–10 000 K in the discharge channel and 2000–4000 K in the igniter. The gas molecules are dissociated and pushed out of the igniter, forming a 'heating core' with high temperature (2000–3000 K) and chemical activity following a wavefront propagating with a velocity of 750–875 m s⁻¹. The calculated evolution of the heating core agrees well with the ICCD measurements. It is found that the 'ladder-like' structure does not affect the penetration depth or expansion radius of the heating core, but leads to a complex vortical flow that allows for chemical activity species to be brought out into the ambient gas.

Keywords: plasma, numerical model, spark jet igniter, multi-physical process

(Some figures may appear in colour only in the online journal)

1. Introduction

Combustion starts with the ignition. A common way to ignite combustible mixtures is to energize the gas/fuel mixture with electrical discharges. By applying high voltage pulses to the electrodes of an igniter, a gas discharge plasma region filled with large quantities of heat and energetic charged particles (e.g. electrons, ions, excited molecules and radicals, etc) will be generated to launch the combustion processes. The effects of gas discharge plasma on combustion and ignition have been

summarized as three categories [1]: the thermal effects, the chemical effects, and the transport effects. There exist several kinds of igniter types, for example, the thermal-effect-based spark plug igniter, the chemical-effects-enhanced nanosecond pulse plasma igniter [2, 3], and the plasma spark jet igniter [4, 5], etc.

The plasma spark jet igniter is a promising igniter configuration as it combines the aforementioned three effects. The working procedures of a spark jet igniter are very similar to a plasma synthetic jet actuator used in the field of plasma-assisted flow [6–11]. A typical spark jet igniter consists of a discharge chamber with one side open that contains two electrodes separated by an insulator. By applying a high voltage

* Authors to whom any correspondence should be addressed.

pulse on the electrodes, the gas in the chamber will be heated and dissociated by the high-temperature plasma discharge, forming a jet flowing out for ignition.

Numerical models are essential for the design and optimization of the igniter. However, the multi-physics processes coupling gas discharges, fluid dynamics, and combustion chemistry make simulation a challenging task. A series of models coupling nonequilibrium plasma and fluid flow have been built to study plasma synthetic jet actuators [12] and surface dielectric barrier discharge actuators [13, 14]. Nusca *et al* [15] simulated the reaction kinetics of a plasma jet after discharge and described the main characteristics of the jet. The discharge process is neglected. Simulation of the spark ignition was conducted by Thiele *et al* [16], taking into account the reaction and transport of charged particles. Recently, the nanosecond spark plug was also self-consistently modeled, coupling gas discharge and combustion processes [17, 18].

The spark jet igniter, however, has not yet been fully studied. Only a reference analytical model can be found in [9], which predicts only the hydrodynamic effects of a plasma synthetic jet actuator with a similar geometry to the spark jet igniter. The work aims to build a multi-physics model describing the discharge plasma and gas hydrodynamics inside the spark jet igniter in a self-consistent manner. With the help of this model, the properties of gas discharge propagation and heating, the evolution of the heating core, and the influence of geometry are also studied.

2. Model description

2.1. The geometry and working process

The schematic of the spark jet igniter and the simplified geometry for modeling are plotted in figures 1(a) and (b). The igniter consists of a cathode at the bottom, an anode around the orifice, and dielectric insulation separating the two electrodes. The external radius of the igniter is 9.5 mm. The radius of the outlet is 4 mm and the depth of the cavity is 10 mm.

The schematic of the igniter discharge experiment system is presented in figure 2. A home-made power supply is used to generate a peak-to-peak voltage of 8 kV, the stored energy of each cycle is 12 J and a maximum discharge frequency of 10 Hz. A digital oscilloscope (Tektronix DPO4104), a 75 MHz high-voltage probe (Tektronix P6015A) and a 120 MHz current probe (Pearson 6600) were used to record the voltage and current profiles. A high-speed camera (Phantom v2512) was used to capture the evolution of the 'bright' heating core.

The voltage and current waveform of the spark jet igniter in one discharge cycle are measured and plotted in figure 3. The working process of the spark jet igniter can be divided into three stages: the discharge propagation stage, the heating stage and the jet stage:

- (i) The discharge propagation stage (0–56 ns): the voltage rises sharply to 3000 V in tens of nanoseconds, leading to the initiation of streamer discharges.
- (ii) The gas heating stage (56 ns–14 μ s): once a conductive path is established between electrodes, the voltage drops

quickly back to 500 V. starting from this stage, the current value and energy deposition increase quickly.

- (iii) The jet stage (56 ns–18 μ s): the heated gas expands and flows out of the igniter in the following tens of microseconds. In this time duration, we mainly focus on the hydrodynamic responses and mass transport outside the igniter, as the gas heating characteristics are decoupled and precalculated in stage (ii).

In the discharge propagation stage, the discharge is in a state of thermal and chemical nonequilibrium; the gas heating stage can be considered as an equilibrium arc discharge with gas heating following Ohm's law; in the jet stage, the focus is the hydrodynamic expansion of the reactive flow and corresponding reactive species. In this work, we simulate these stages separately and couple each stage by defining the initial distribution of temperature and pressure for the next stage.

2.2. Equations for the discharge propagation stage

The nonequilibrium plasma generated during the discharge propagation stage is modeled using the plasma solver *PASS-KEy* (PARallel Streamer Solver with KinEtics) [19]. The detailed numerical method and validations can be found in [20, 21]. In this work, we briefly introduce the equations solved.

A set of drift–diffusion equations are solved for the charged particles:

$$\frac{\partial n_i}{\partial t} + \nabla \cdot \Gamma_i = S_i + S_{ph}, \quad i = 1, 2, 3, \dots, N_{\text{total}}, \quad (1)$$

$$\Gamma_i = -D_i \nabla n_i - \left(\frac{q_i}{|q_i|} \right) \mu_i n_i \nabla \phi, \quad i = 1, 2, 3, \dots, N_{\text{charge}}, \quad (2)$$

where n_i is the number density of species, q_i is the charge of species and S_i is the source term of detailed chemical reactions. S_{ph} is the photo-ionization source term. D_i and μ_i are the diffusion coefficient of an electron and the mobility of charged species i , which are tabulated before calculation. Photoionization affects the propagation and morphology of the volumetric streamer. An efficient photoionization model based on three exponential Helmholtz equations [22, 23] is used to calculate S_{ph} .

The kinetics scheme is the same as that in [24], which is a combination of a kinetics scheme used for streamer propagation [25] and fast gas heating (FGH) [26]. In total, 15 species (electron, N_2 , $\text{N}_2(\text{A}^3\Sigma_u^+)$, $\text{N}_2(\text{B}^3\Pi_g)$, $\text{N}_2(\text{C}^3\Pi_u)$, N_2^+ , N_4^+ , O_2 , O , $\text{O}(^1\text{D})$, O_2^+ , O_4^+ , O^- , O_2^-) and 34 reactions are considered. The combustive mixture is not taken into account in this study for the following reasons:

- (i) the igniter studied in this work must be installed on the wall of a combustion chamber perpendicular to the flow direction, the gaseous fuel can hardly enter the igniter cavity in the flow field, as the cavity pressure is relatively higher. Thus, we assume there is no combustion reaction inside the igniter, the ignition process is triggered mainly outside the

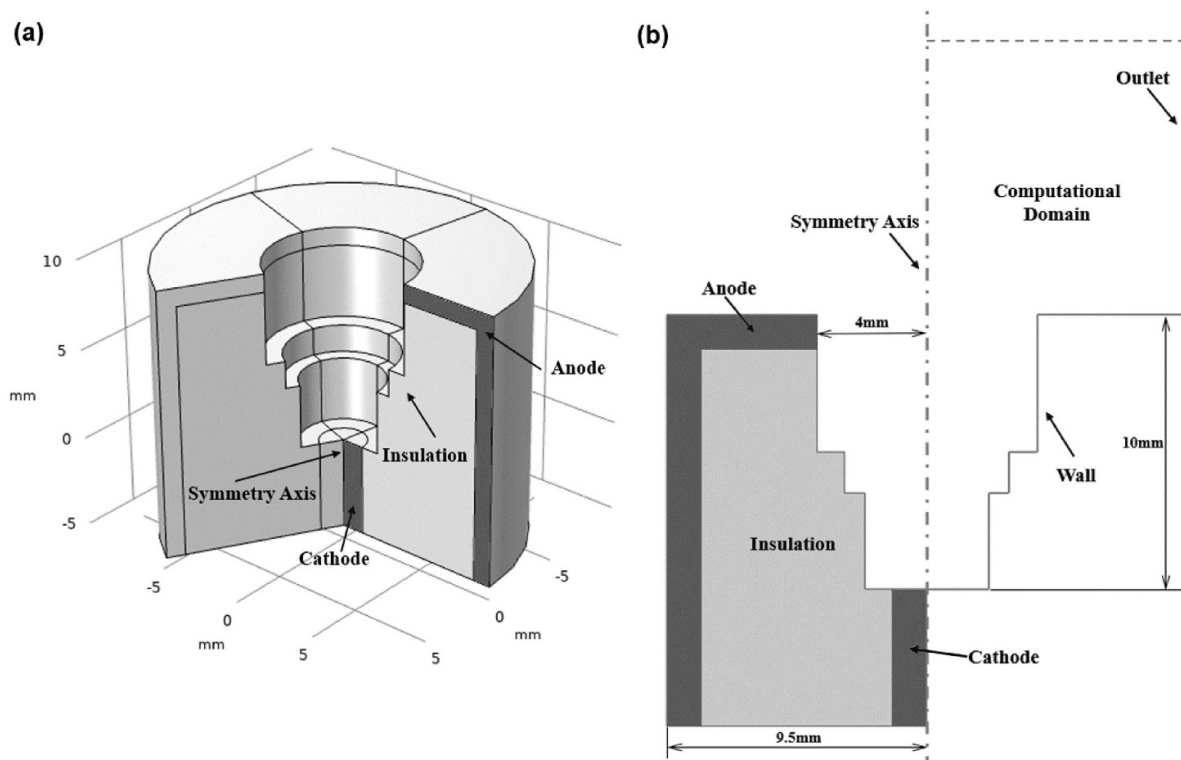


Figure 1. The schematic of the spark jet igniter model. (a) The 3D view of the igniter computational domain. (b) The 2D view of the structure (left of the z -axis) and computational domain (right of the z -axis) of the igniter.

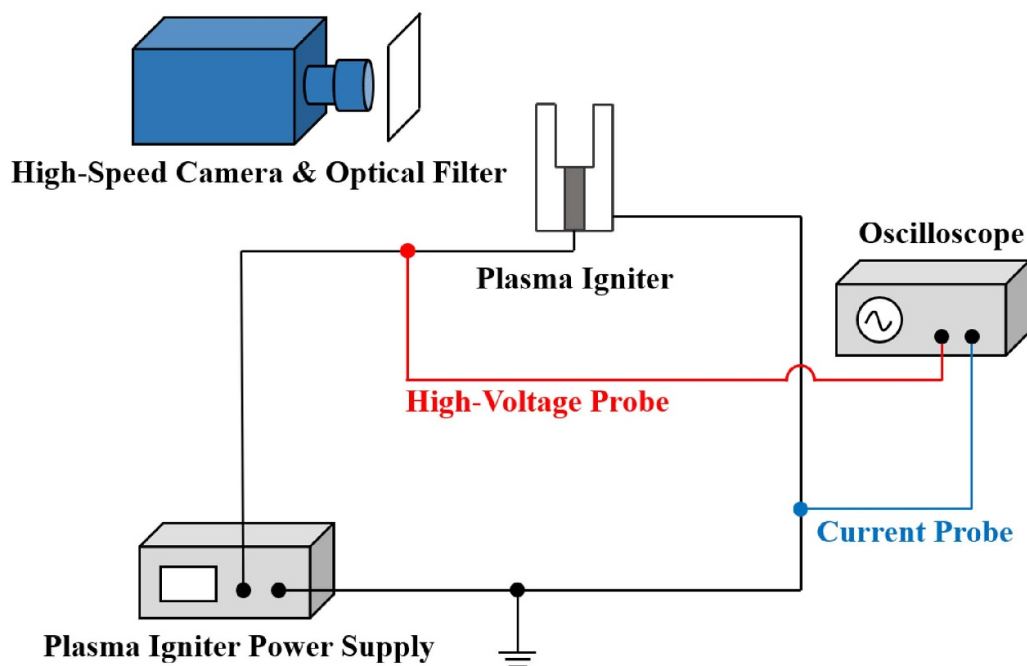


Figure 2. Schematic of the experimental setup.

cavity when the heated gas flows out, forming an ignition kernel;

- (ii) The combustive species, before the gas is heated, are usually large molecules in liquid state. The major component of gas is air instead of spray fuel cloud, which is mainly

liquid. The fuel steam is supplied outside the igniter but its density is rather low in the cavity;

- (iii) This igniter is designed to ignite macromolecular kerosene (for example C5–C12) in engines, however, the elementary data (cross sections, reaction rates and kinetics

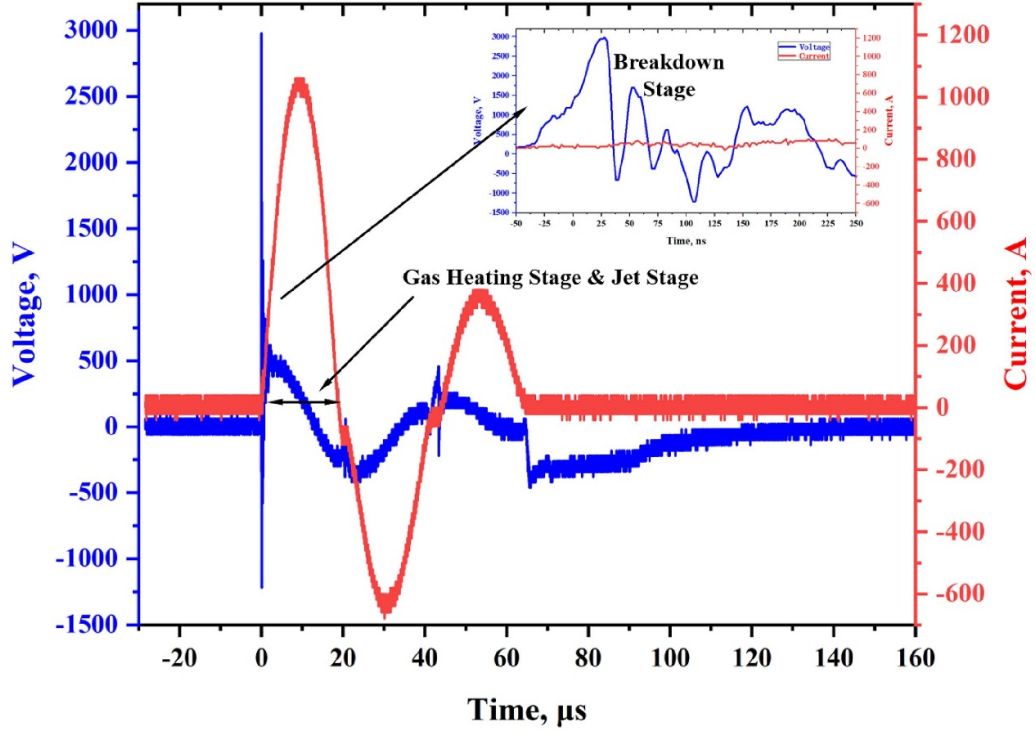


Figure 3. The measured voltage and current waveform of the spark jet igniter in one discharge cycle.

schemes) for these macromolecules (steam in the gas state) are still under development.

The mean electron energy is calculated based on local mean energy approximation (LMEA) [21]:

$$\frac{\partial(n_e \epsilon_m)}{\partial t} + \nabla \cdot \Gamma_\epsilon = -|q_e| \cdot \Gamma_\epsilon \cdot \mathbf{E} - P(\epsilon_m), \quad (3)$$

$$\Gamma_\epsilon = -n_e \epsilon_m \mu_\epsilon \mathbf{E} - D_\epsilon \nabla(n_e \epsilon_m), \quad (4)$$

where n_e is the electron number density, ϵ_m is the mean electron energy, Γ_ϵ is the flux term, μ_ϵ and D_ϵ are the electron energy mobility and diffusion coefficients respectively. q_e is the elementary charge and \mathbf{E} is the electric field, $P(\epsilon_m)$ represents the electrons collision power lost calculated by BOLSIG+ software [27–29].

Poisson's equation is solved for the electric potential and field:

$$\nabla(\epsilon_0 \epsilon_r \nabla \phi) = -\sum_{i=1}^{N_{charge}} q_i n_i, \quad (5)$$

$$\mathbf{E} = -\nabla \phi, \quad (6)$$

where ϵ_0 is the permittivity of vacuum space, ϵ_r is the relative permittivity of air.

Euler equations are used to solve viscid fluid flow dynamics for gas temperature evolution:

$$\frac{\partial \mathbf{U}}{\partial t} + \frac{\partial \mathbf{F}}{\partial t} + \frac{\partial \mathbf{G}}{\partial t} = \mathbf{S}, \quad (7)$$

$$\mathbf{U} = \begin{bmatrix} \rho \\ \rho u \\ \rho v \\ e \end{bmatrix}, \mathbf{F} = \begin{bmatrix} \rho u \\ p + \rho uu \\ \rho uv \\ (e + p)u \end{bmatrix}, \mathbf{G} = \begin{bmatrix} \rho v \\ \rho uv \\ p + \rho vv \\ (e + p)v \end{bmatrix},$$

$$\mathbf{S} = \begin{bmatrix} 0 \\ 0 \\ 0 \\ S_{heat} \end{bmatrix}, \quad (8)$$

where ρ is the density of gas, different from charged particle densities solved in equation (1), p is the gas pressure, u and v are the velocity components, e is the total energy, S_{heat} is calculated through the sum of the FGH energy released mainly through quenching of excited species [24]. The FGH is the major heating source in the nanoseconds timescale. The electro-hydro dynamics force is not considered.

The closure model used for the Euler equations by gas state equation:

$$p = (\gamma - 1) \rho i, \quad (9)$$

where $i = e - (u^2 + v^2)/2$ is the specific internal energy, γ is the specific heat ratio.

The details of the coupling between flow and plasma is illustrated in [30]. In short, the coupling can be described as:

- (i) For weakly ionized plasma, most species (excited species and charged particles) are rather low in concentration and are not coupled. O atoms, N₂ and O₂ are chosen to be coupled.

- (ii) In each time step, the densities calculated by the plasma equations are transferred to the fluid equations, for each coupled species we solve a continuity equation, and the sum of the density is used for the momentum equation.
- (iii) The updated density is then transferred back to the plasma equation for calculation of E/N et al. At the end of the discharge propagation stage, the plasma will transition from streamer discharge mode to spark discharge mode, that is, a plasma channel will be formed between cathode and anode [31].

2.3. Equations for the gas heating stage

After the conductive plasma channel was established, the discharge soon transforms into the equilibrium arc in a micro-second time scale. Modeling the streamer–spark–arc transition from nonequilibrium to equilibrium mode is still a challenging task not well solved. Pioneering works modeling the thermalization can be found in [11, 17]. In our work the thermal discharge lasts a much longer time, requiring a quite large change in the model (from a two-temperature model with fixed EEDF to a single temperature model with the magnetic field, thermal chemistry and strongly changed EEDF), thus we skip the transition moment, the commercial software COMSOL Multiphysics is used for the thermal arc gas heating stage. Navier–Stokes equations and electromagnetic equations are solved in this stage:

$$\frac{\partial \rho}{\partial t} + \nabla \cdot (\rho \mathbf{u}) = 0, \quad (10)$$

$$\frac{\partial \rho \mathbf{u}}{\partial t} + \rho \mathbf{u} \cdot \nabla \mathbf{u} = \nabla \cdot \{-p\mathbf{I} + [\mu(\nabla \mathbf{u}) + (\nabla \mathbf{u})^T]\} + \mathbf{j} \times \mathbf{B}, \quad (11)$$

$$\rho C_p \frac{\partial T_g}{\partial t} + (\rho C_p \nabla T_g \cdot \mathbf{u}) - \nabla \cdot (k \cdot \nabla T_g) = Q_p + Q_{Joule} + Q_h + Q_{rad} + \tau : \nabla \mathbf{u}, \quad (12)$$

where ρ is the density and \mathbf{u} is the velocity of the fluid. p is pressure, μ is the viscosity of the fluid, \mathbf{I} is the identity matrix and $F_L = \mathbf{j} \times \mathbf{B}$ is the Lorentz Force term contributing to the momentum conservation equation. C_p is the specific heat capacity of the gas, T_g is the gas temperature, k is the thermal conductivity.

The energy source terms include: the pressure power Q_p , the Joule heating term $Q_{Joule} = \mathbf{j} \cdot \mathbf{E}$, the enthalpy transfer term Q_h and the radiation power $Q_{rad} = 4\pi\epsilon_r \cdot \epsilon_r$ is the radiation coefficient per unit volume [32], $\tau : \nabla \mathbf{u}$ is the viscous dissipation term.

Electromagnetic equations are solved to provide the magnetic and electric field:

$$\mathbf{E} = -\nabla V, \quad (13)$$

$$\mathbf{j} = \sigma(\mathbf{E} + \mathbf{u} \times \mathbf{B}), \quad (14)$$

Table 1. Boundary conditions in gas heating stage.

	Fluid field	Heat transfer	Electric field	Magnetic field
Cathode	0	$\mathbf{n} \cdot \nabla T = 0$	P	$\mathbf{n} \times \mathbf{A} = 0$
Wall	0	$\mathbf{n} \cdot \nabla T = 0$	$\mathbf{n} \cdot \nabla \phi = 0$	$\mathbf{n} \times \mathbf{A} = 0$
Anode	0	$\mathbf{n} \cdot \nabla T = 0$	$V = 0$	$\mathbf{n} \times \mathbf{A} = 0$
Outlet	$p = 1 \text{ atm}$	$\mathbf{n} \cdot \nabla T = 0$	$\mathbf{n} \cdot \nabla \phi = 0$	$\mathbf{n} \times \mathbf{A} = 0$

\mathbf{n} is the unit vector perpendicular to the boundary.

$$\nabla \cdot \mathbf{j} = 0, \quad (15)$$

$$\nabla \times \mathbf{B} = \mu_0 \mathbf{j}, \quad (16)$$

where σ is the electrical conductivity and \mathbf{B} is the magnetic induction, $\mathbf{B} = \nabla \times \mathbf{A}$. \mathbf{A} is the magnetic vector potential. The gas physical parameters (μ , C_p , k , σ) are taken from the gas discharge plasma database (GPLAS) [33]. The boundary conditions used by the model are shown in table 1.

The boundary condition for electric field at the cathode is set according to the mean power P calculated from voltage and current waveforms, see equation (17):

$$P = \int_{t_{\text{start}}}^{t_{\text{end}}} UI dt / (t_{\text{end}} - t_{\text{start}}). \quad (17)$$

The electron number density is not solved in the gas heating (or arc discharge) stage, but can be roughly estimated from the electrical conductivity assuming local temperature equilibrium (LTE):

$$n_e = \sigma(T_g, p) / (\mu_e \cdot e), \quad (18)$$

where μ_e is the electron mobility which is calculated by BOLSIG+ [34], e is the basic charge and n_e is the electron density. The electrical conductivity is a derived quantity that depends on the electron mobility μ_e and electron number density n_e , but under the LTE assumption, the electrical conductivity can be considered as a function of gas temperature and pressure [35, 36]. The data can be calculated and stored in databases (e.g. the GPLAS). This estimation method is rough, especially in the non-LTE region of the computational domain.

2.4. Equations for the jet stage

The jet stage is also studied within the framework of COMSOL Multiphysics. The evolution of species is calculated taking into account chemical reactions. Drift-diffusion equations for each species are solved:

$$\frac{\partial n_i}{\partial t} + \nabla \cdot \Gamma_i + \nabla \cdot (\mathbf{u} n_i) = S_i, \quad (19)$$

where $\Gamma_i = -D_i \nabla n_i$ is the diffusion flux of species i , S_i is the source term determined by reaction coefficients k and species number density n , D_i is the diffusion coefficient [37]:

Table 2. Boundary conditions in the jet stage.

	Fluid flow	Heat transfer	Flux
Cathode	0	$\mathbf{n} \cdot \nabla T = 0$	$-\mathbf{n} \cdot \Gamma_i = 0$
Wall	0	$\mathbf{n} \cdot \nabla T = 0$	$-\mathbf{n} \cdot \Gamma_i = 0$
Anode	0	$\mathbf{n} \cdot \nabla T = 0$	$-\mathbf{n} \cdot \Gamma_i = 0$
Outlet	$p = 1 \text{ atm}$	$\mathbf{n} \cdot \nabla T = 0$	$-\mathbf{n} \cdot n_i = 0$

\mathbf{n} is the unit vector perpendicular to the boundary.

$$D_i = \frac{1 - Y_i}{\sum_{j \neq i} (X_j / D_{ij})}, \quad (20)$$

$$D_{ij} = CT^{3/2} \frac{\sqrt{1/m_{ij}}}{\rho \sigma_{ij}^2 \Omega(1, 1)^*}, \quad (21)$$

where D_{ij} is the binary diffusion coefficients, Y_i is the mass fraction of species i , X_j is the mole fraction of species j . $C = 1.883 \times 10^{-2}$, $m_{ij} = \frac{m_i m_j}{m_i + m_j}$ is the reduced mass of the species i and j , σ_{ij} is the characteristic length [37], $\Omega(1, 1)^*$ is the collision integral which depends on the gas temperature taken from [38].

The momentum conservation equation and energy conservation equation in the gas heating stage are modified for the compressive flow and reactive flow:

$$\frac{\partial \rho \mathbf{u}}{\partial t} + \rho \mathbf{u} \cdot \nabla \mathbf{u} = \nabla \cdot \left\{ -p \mathbf{I} + [\mu(\nabla \mathbf{u}) + (\nabla \mathbf{u})^T] - \frac{2}{3} \mu(\nabla \cdot \mathbf{u}) \mathbf{I} \right\}, \quad (22)$$

$$\rho C_p \frac{\partial T_g}{\partial t} + (\rho C_p \nabla T_g \cdot \mathbf{u}) - \nabla \cdot (k \cdot \nabla T_g) = Q_p + Q_{\text{reaction}} + \tau : \nabla \mathbf{u}, \quad (23)$$

where Q_{reaction} is the heat source term contributed by detailed chemical reactions presented in table 3. In the jet stage we do not solve for the Joule heating term. The boundary conditions are summarized in table 2.

A simplified chemistry scheme is used for this stage. The chemistry set is retrieved from [39] and presented in table 3. The scheme includes the main reaction pathways for the production of O atoms due to air pyrolysis in the high-temperature region.

2.5. Heat sources and assumptions in the model

The physical processes and corresponding models differ, here we clarify the heat sources used and major assumptions made in each stage.

The heat source terms for equations (8), (12) and (23) are summarized as follow:

- (i) The discharge propagation stage: the source term is calculated by summing the enthalpy changes of all the FGH reactions, the relaxation of vibrationally excited states are not included in this short time scale.

- (ii) The gas heating stage: we assume the plasma is LTE, the source term consists of the pressure power, the Joule heating power, enthalpy transport, radiation power and viscous dissipation loss.

- (iii) The jet stage: we solved a convection-reaction system, the source term consists the pressure power, reaction heat power and viscous dissipation loss.

The assumptions made for stages (i), (ii) and (iii) are:

- (i) The discharge propagation stage:
 - (a) The plasma is in chemical and thermal nonequilibrium. The EEDF, electron swarm parameters are precalculated based on LMEA and the two-terms Boltzmann approximation.
 - (b) The fluid dynamics is solved based on Euler's equations. The effect of viscosity can be neglected in the short time period.
- (ii) The gas heating stage:
 - (a) The plasma is in thermal equilibrium. The spark-to-arc transition is skipped, as the temperature increase and molecules dissociation occurs mainly in the arc stage in this igniter.
 - (b) The fluid dynamics is described based on N-S equations. The flow is viscous and laminar.
- (iii) The jet stage:
 - (a) The plasma discharge process in the jet stage is not considered. Only the hydrodynamic responses and mass transport outside the igniter are studied with input of the gas heating characteristics from stage (ii).
 - (b) The fluid dynamics is described based on N-S equations, too. The flow is also viscous and laminar: the turbulent effects are not considered due to the regions with high Reynolds number is limited in the shock front, after the shock the turbulent effects can be neglected.

3. Results and discussions

The discharge characteristics, the flow responses and their coupling will be discussed in this section to reveal how a spark jet igniter works over a single work cycle. The role of geometry design on the performance of the igniter is then discussed based on the modeling results.

3.1. The streamer and arc discharge evolution

The discharge characteristics differ in the period before and after the discharge gap closing. The evolutions of electron density and electric field during discharge propagation are shown in figures 4(a)–(d) and 5(a)–(d), respectively. A discharge streamer starts from the edge of the cathode at the bottom, directed towards the anode in the first 20 ns (figure 4(a)) with a peak field of 400–500 Td in the ionization head (figure 5(a)). It is important to note that the applied voltage to this igniter is no larger than 3 kV, while usually a voltage of tens of kilovolts is required to close the gap between the anode and cathode at atmospheric pressure: e.g. for a 1 cm

Table 3. Chemical process taken into account in the jet stage.

Chemical process	M	Rate coefficient ^b ($k = A \cdot T^b \cdot \exp^{-E/RT}$)
$N_2 + O_2 \leftrightarrow 2NO$	/	$k_1 = 9.1 \times 10^{24} T^{-2.5} e^{-128500/RT}$
$N_2 + O \leftrightarrow NO + N$	/	$k_2 = 7 \times 10^{24} T^{-2.5} e^{-128500/RT}$
$O_2 + N \leftrightarrow NO + O$	/	$k_3 = 1.34 \times 10^{10} T^1 e^{-7080/RT}$
$O_2 + M \leftrightarrow 2O + M$	N, NO	$k_4 = 2.5 \times 10^{11} T^{0.5} (118000/RT)^{1.5} e^{-118000/RT}$
$O_2 + M \leftrightarrow 2O + M$	N ₂	$2k_4$
$O_2 + M \leftrightarrow 2O + M$	O ₂	$9k_4$
$O_2 + M \leftrightarrow 2O + M$	O	$25k_4$
$N_2 + M \leftrightarrow 2N + M$	NO, O, O ₂	$k_5 = 1.7 \times 10^{12} T^{0.5} (224900/RT)^1 e^{-224900/RT}$
$N_2 + M \leftrightarrow 2N + M$	N ₂	$(4.2/1.7)k_5$
$N_2 + M \leftrightarrow 2N + M$	N	$(3.2/1.7)k_5$
$NO + M \leftrightarrow N + O + M$	O ₂ , N ₂	$k_6 = 7.0 \times 10^{10} T^{0.5} (150000/RT)^2 e^{-15000/RT}$
$NO + M \leftrightarrow N + O + M$	NO, O, N	$20k_6$

^a The reference of chemical process and reaction rate coefficients is paper [39].

^b The rate coefficients are given in $\text{cm}^{-3} \text{s}^{-1}$, $\text{cm}^{-6} \text{s}^{-1}$.

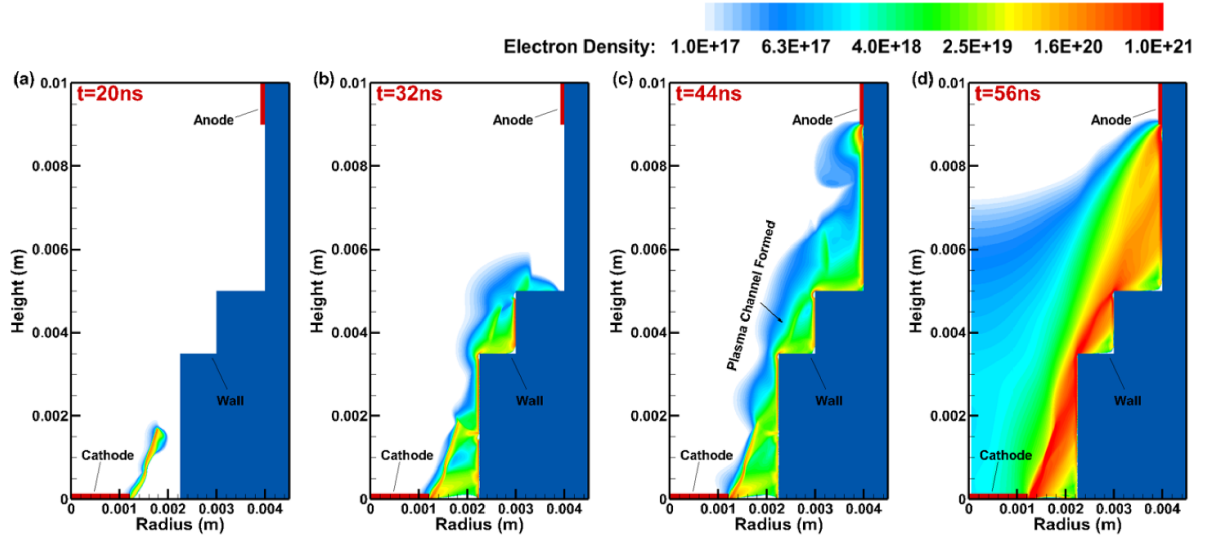


Figure 4. The electron density distribution in the discharge propagation stage. The red parts represent the cathode and anode and the blue part represents the dielectric wall. (a) $t = 20$ ns, (b) $t = 32$ ns, (c) $t = 44$ ns, (d) $t = 56$ ns, unit: m^{-3} .

gap, 13 kV is required to breakdown in a pin-to-plane configuration [40], the 3 kV voltage cannot sustain the streamer to penetrate the gas gap between two electrodes. As a result, after the streamer head propagates 2–3 mm, it stops, changes its direction and attaches to the insulating dielectric at about 32 ns, see figure 4(b).

The attachment of a volumetric streamer to the insulating dielectric has been numerically explained in a recent work [41]: the dielectric is polarized due to the strong electric field in the streamer head, as a result, the electric field between the streamer and the insulating dielectric is enhanced. In this work the motion of charges inside the dielectric is not solved, the streamer will still attach to the dielectric when the electrons in the gap between the dielectric and the streamer body are attracted into the streamer due to net charge in the streamer head. We would prefer the statement ‘the gas between the dielectric and the streamer head is polarized due to the strong electric field’.

After the attachment, the discharge propagation process is dominated by the surface discharge: the surface discharge exhibits a much thinner streamer and higher electric field in the head (figures 5(b) and (c)), making it possible to continue propagating towards the anode, see figures 4(b) and (c). Once the surface streamer approaches the cathode, a positive surface streamer forms near the edge of the anode, and propagates for about 1 mm and connects the negative streamer to form a closed plasma channel at 44 ns, as can be seen in figure 4(c). Here we clearly see that the specially designed dielectric shape can significantly reduce the breakdown voltage between electrodes, or the starting voltage of a sparkjet igniter.

Once the electrodes are connected by the plasma, the remaining electric field on the level of 100–150 Td is still high enough (than the ionization threshold field of air 120 Td) to ionize the gas in the discharge channel, leading to the formation of a spark discharge after 56 ns, as is shown in figure 4(d).

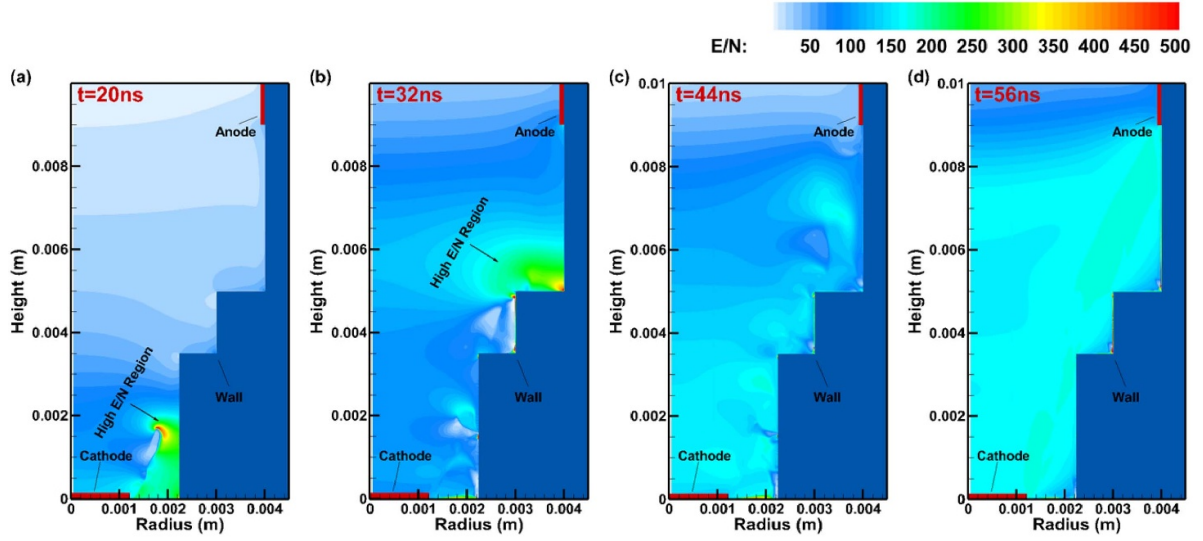


Figure 5. The evolution of reduced electric field E/N in streamer discharge during the discharge propagation stage. The red parts represent the cathode and anode and the blue part represents the dielectric wall. (a) $t = 20$ ns, (b) $t = 32$ ns, (c) $t = 44$ ns, (d) $t = 56$ ns, unit: Td.

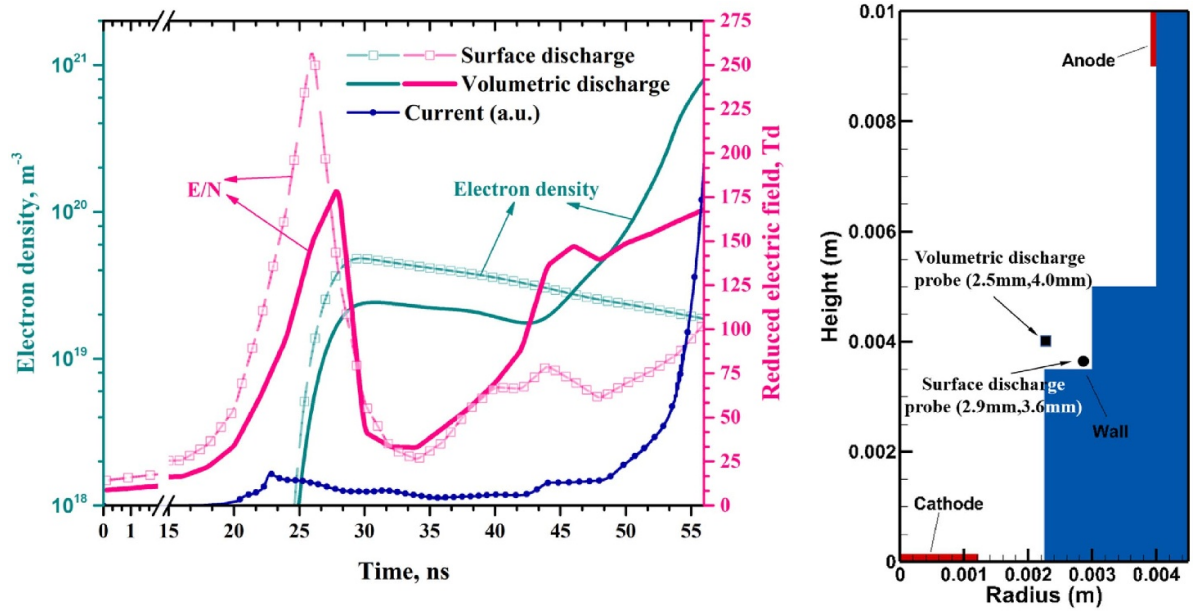


Figure 6. The temporal evolution of the electron density, the reduced electric field and the current value (a.u.), volumetric discharge probe coordinate: (2.5, 4.0 mm), surface discharge probe coordinate (2.9, 3.6 mm).

It is interesting to see that, the shape of the spark channel does not reproduce the previously formed surface streamer channel, instead, the spark discharge connects the two electrodes following the shortest route. An intensified volumetric discharge with a maximum diameter of $170 \mu\text{m}$ is formed. The surface streamer provides the seed electrons for the secondary volumetric discharge, making the secondary discharge looks quite ‘thick’ in the cavity. We zoomed in on the volumetric and surface discharge region and plotted the temporal evolution of the electron density and current in figure 6.

It is seen that the electron density increases twice in the volumetric discharge channel, the first caused by the preionization from surface discharge and the second due to

the gap closing. As the ‘spark’ forms, the current increases dramatically. With the further increase of the voltage, the spark discharge will get intensified, and finally transit into a thermal arc.

The electron density and reduced electric field in the arc stage are estimated using equation (18) in figure 7. The electric field ranges from 25 to 160 Td, much lower than that in the discharge propagation stage. The discharge kinetics at this stage is dominated by temperature instead of the electric field or the electron energy. Note that we can see a ‘streamer-like’ evolution of electron density and electric field in the arc stage, but in the arc stage the ‘propagation’ of the high electron density region and the strong electric field head is not caused by

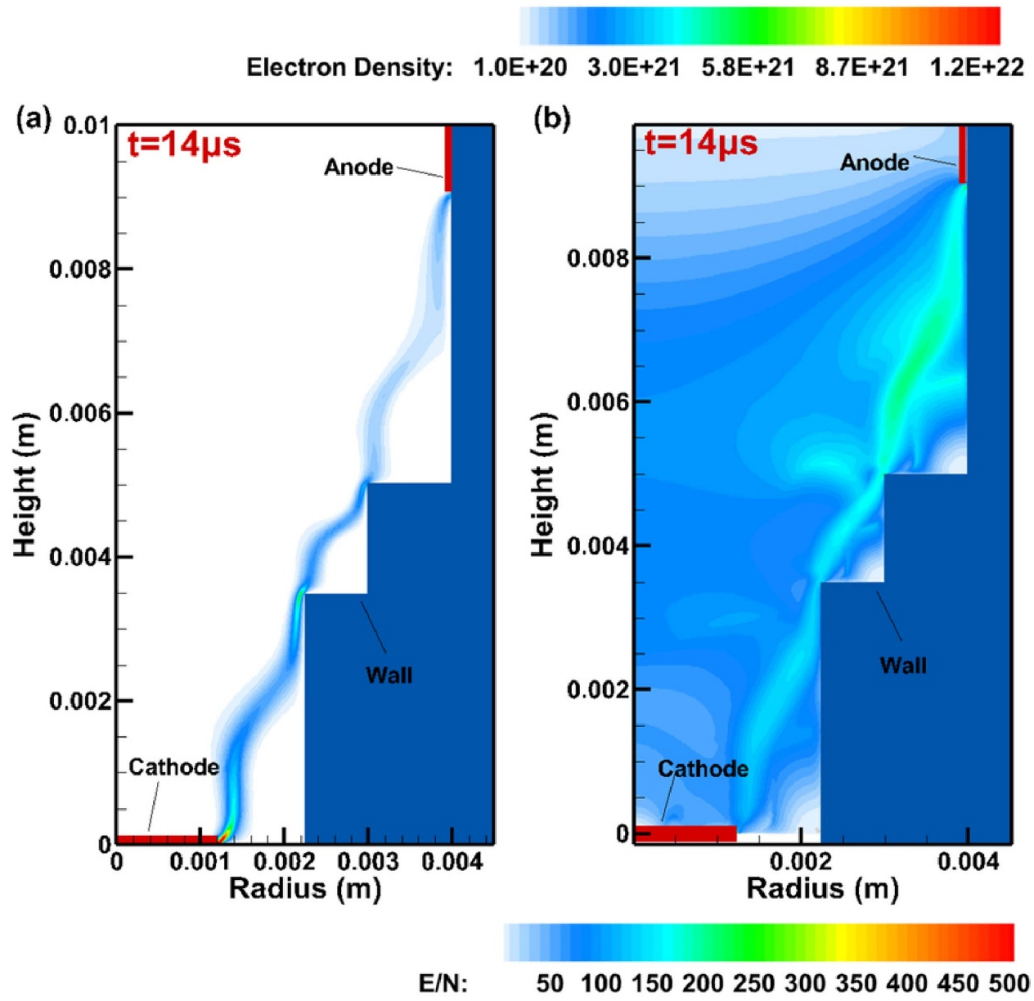


Figure 7. The electron density and reduced electric field distribution at $14 \mu\text{s}$ in gas heating stage: (a) the electron density, unit: m^{-3} and (b) the reduced electric field distribution, unit: Td.

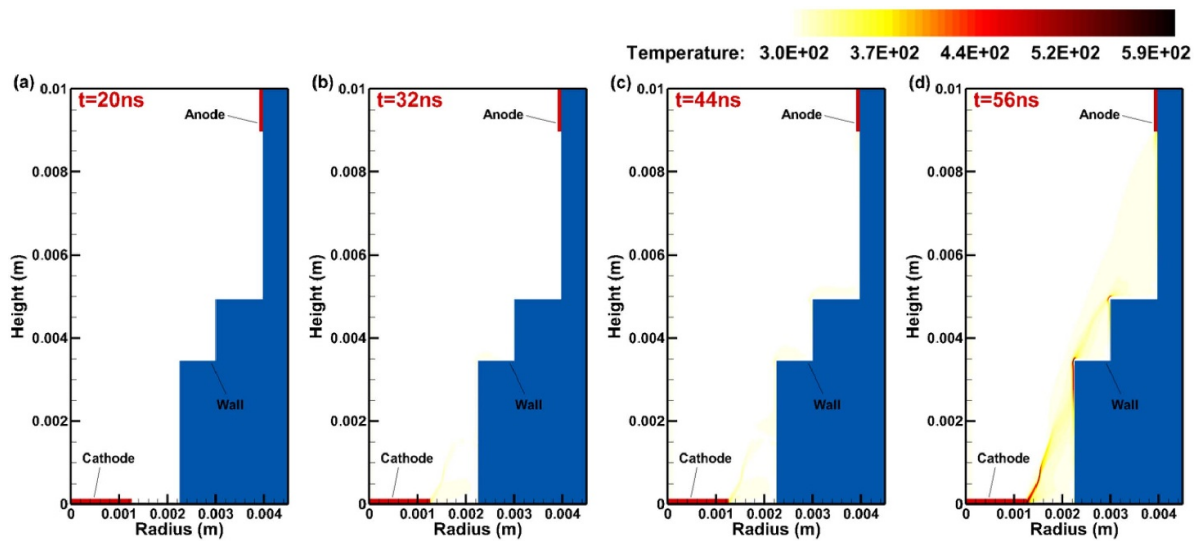


Figure 8. The evolution of temperature in steamer discharge during the discharge propagation stage. After the plasma channel formed, the gas rose rapidly. (a) $t = 20 \text{ ns}$, (b) $t = 32 \text{ ns}$, (c) $t = 44 \text{ ns}$, (d) $t = 56 \text{ ns}$, unit: K.

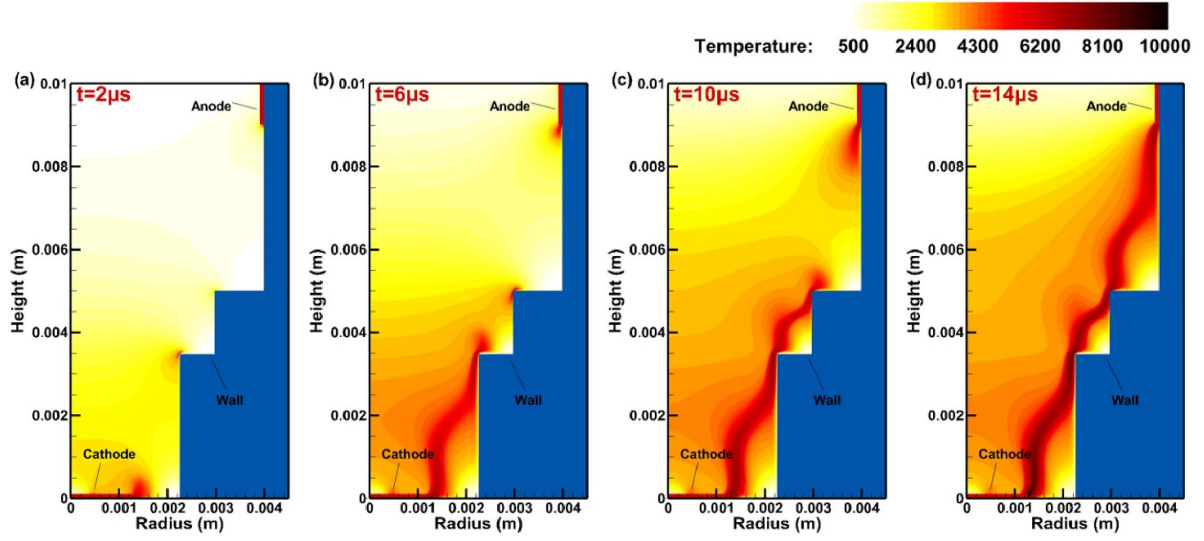


Figure 9. The evolution of temperature in equilibrium arc discharge during the gas heating stage. (a) $t = 2 \mu\text{s}$, (b) $t = 6 \mu\text{s}$, (c) $t = 10 \mu\text{s}$, (d) $t = 14 \mu\text{s}$, unit: K.

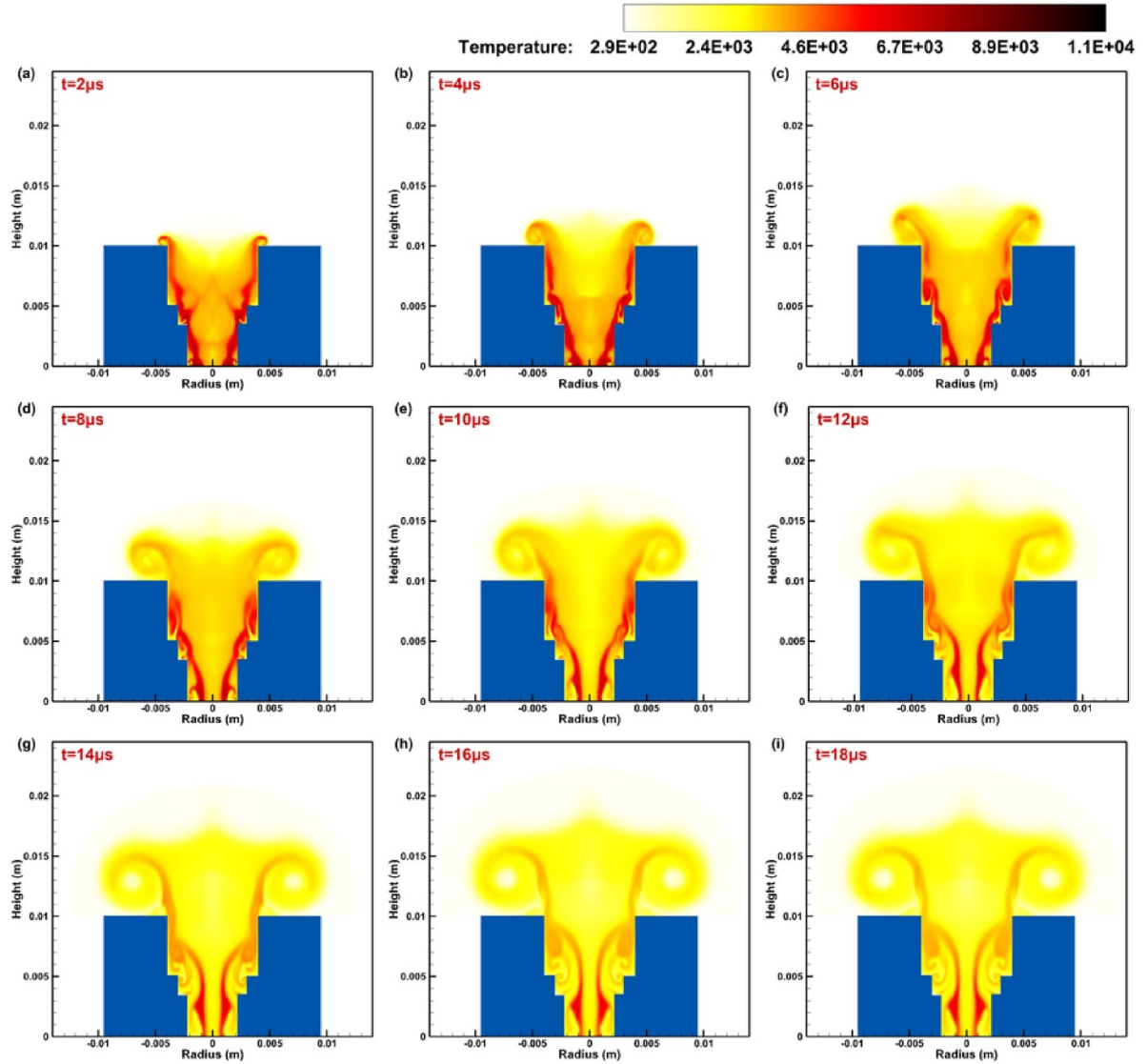


Figure 10. The temperature evolution during the jet stage. The blue represents the igniter. (a) $t = 2 \mu\text{s}$, (b) $t = 4 \mu\text{s}$, (c) $t = 6 \mu\text{s}$, (d) $t = 8 \mu\text{s}$, (e) $t = 10 \mu\text{s}$, (f) $t = 12 \mu\text{s}$, (g) $t = 14 \mu\text{s}$, (h) $t = 16 \mu\text{s}$, (i) $t = 18 \mu\text{s}$, unit: K.

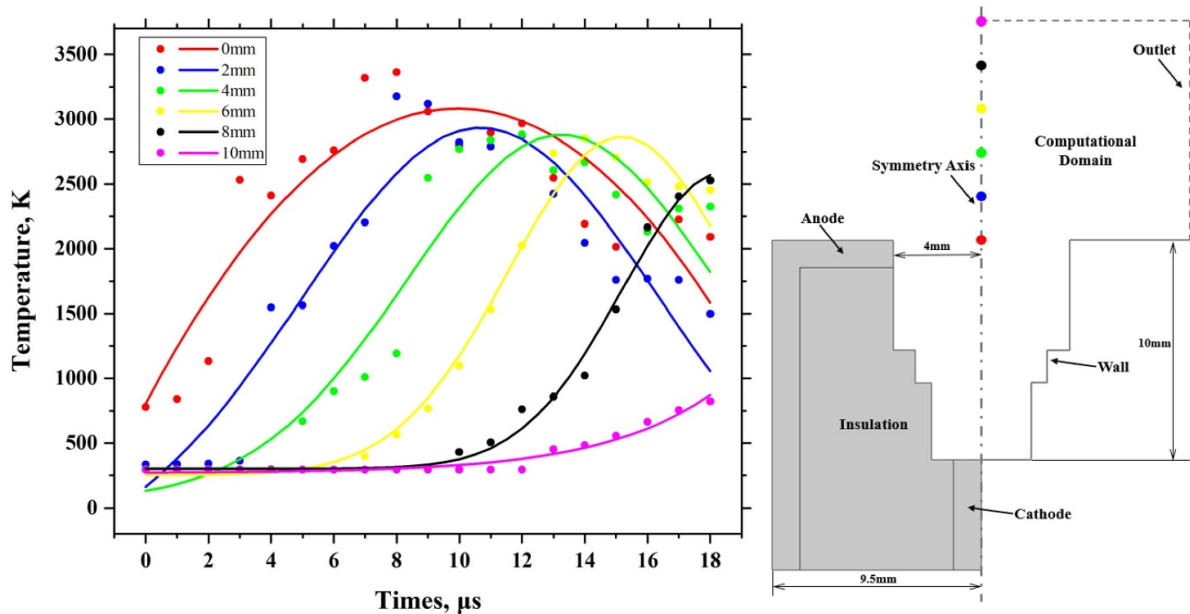


Figure 11. The temperature at different positions on the axis during the jet stage. The points on the igniter axis represent different positions to collect data. The dots represent the original data and the curves are the fitting result, unit: K.

charge separation of electrons and ions, but by the expansion of the heated/high conductivity region.

The discharge propagation process plays the role of connecting the two electrodes in tens of nanoseconds and forming a high conductivity region. Then the majority of the energy is transferred into the gas in tens of microseconds in the spark–arc discharge along the high conductivity region. The direct consequence of the discharge in the igniter is gas heating and chemical reactions. The following section will discuss in detail the characteristics of gas heating and the reactive jet.

3.2. Hydrodynamics evolution of the heating core

In this section, we focus on the fluid response caused by igniter discharge, including the evolution of jet temperature, pressure, mass and O radical density. Temperature is the key parameter linking the discharge propagation stage, the gas heating (arc discharge) stage and the jet stage. The spatial–temporal evolution of the temperature in both stages have been plotted in figures 8(a)–(d) and 9(a)–(d).

In the streamer discharge propagation stage in the first 56 ns, the deposited energy is 2 mJ, 0.1% of the total deposited energy. The electron energy is transferred into the gas molecules mainly through the fast quenching of excited nitrogen molecules by oxygen molecules. The fraction of discharge energy converted to gas heating depends on the electric field in the plasma channel. In the studied case ($E/N = 150$ – 200 Td), the efficiency is at the level of 20%–25%, leading to a rapid gas temperature increase of 70 K in the streamer stage (figures 8(a)–(c)) and 200 K at the beginning of the spark stage (figure 8(d)). This temperature increase has tiny effects on the ignition of the combustible mixture, but the ultrafast heating process in the nanosecond timescale decides the shape of the heating channel in the arc stage.

The energy deposition happens mainly in the arc discharge stage in a microsecond timescale. The high conductivity plasma region between electrodes results in a current value of thousands of Amperes and a Joule heating energy of 2.95 J, 1500 times the energy deposited in the discharge propagation stage, leading to a temperature rise of 7000–10 000 K in the arc channel and 2000–4000 K in the igniter hole, as shown in figures 9(a)–(d). The high energy deposition and following temperature rise and gas compression will strongly affect the species composition and hydrodynamics processes of this spark jet igniter in a longer time scale.

The evolution of temperature in the jet flow is shown in figures 10(a)–(i). The starting time moment is selected as the time when all the discharge energy has been deposited into the gas. The heated region has its highest temperature of 9000 K along the arc channel and the average temperature of 2000–3000 K inside the igniter (figure 10(a)). The heated gas inside the igniter expands into the ambient air from the exit, forming a typical vortex flow outside in 20 μ s. The penetrating depth of the heating core is 1 cm, and the vortex structure leads to a heating radius of 1 cm, and the average temperature of the heating core outside the igniter is 1500–2000 K at 18 μ s after discharge, see figure 10(i). The temporal evolution of the temperature in the heating core at $z = 0, 2, 4, 6, 8$ and 10 mm (see figure 11(b)) are probed and drawn in figure 11(a) as separate dots. It is clearly seen that the temperature of the heating core reaches the peak value (2500–3000 K) in 8 μ s, mainly in the time duration between 10 and 16 μ s after the heated gas starts flowing outside.

It is difficult to perform experimental diagnostics inside the assembled spark igniter. We captured the evolution of the luminous heating core using an ICCD camera to obtain top and front views and compared the shapes of this lighting core with the calculated temperature evolution as an indirect validation,

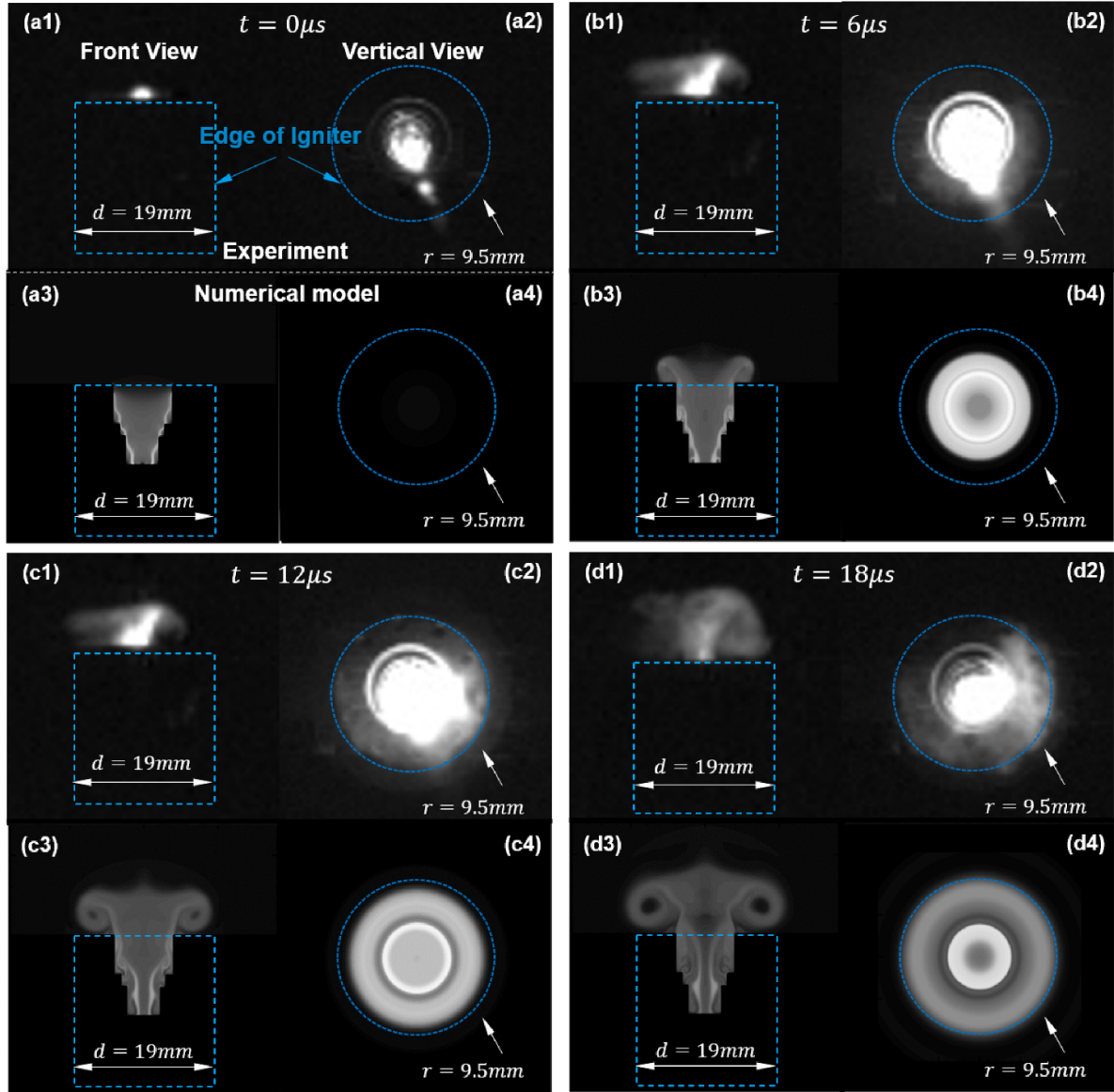


Figure 12. Comparison of experimental and calculated images of the heating core at (a) $t = 0 \mu\text{s}$, (b) $t = 6 \mu\text{s}$, (c) $t = 12 \mu\text{s}$, (d) $t = 18 \mu\text{s}$. The calculated heating core is represented by the temperature distribution. For each time moment, the first row shows the captured heating core (front and top view, respectively), the second row shows the calculated results at the same moment. The blue dash boxes describe the boundaries of the igniter, the $0 \mu\text{s}$ is selected as the time moment when the current signal triggered the camera.

see figures 12(a)–(d). In $18 \mu\text{s}$, the gas heating core flows out of the igniter, forming a ‘mushroom’ structure with comparative penetration depth and radius. The calculated temperature distribution reproduces well the measured evolution of the lighting and heating core at different time moments: the propagation velocity of $750\text{--}875 \text{ m s}^{-1}$ and the vortex radius of 2.5 mm with the hottest region near the center.

Note that there is always a hollow region in the calculated distribution of temperature from the top view while in the measured images the igniter center is always bright: in the experiment, the picture is captured through line integration of the emission along the vertical line instead of the slice way in the simulation. We also have to note that the discharge channel calculated by this two dimensional symmetric model is, in essence, a conical-like surface instead of an arc filament. This

is the reason why in the experimental images there is always a local bright region shown in the top view. This model cannot capture the very thin filamentary arc as well as the brightest region (with the highest temperature) in the experiment. Despite this dimensional difference, the model ensures the same energy deposition as in the experiment inside the igniter, thus the average characteristics of the reactive jet flow (temperature, velocity and species density) of the igniter can still be represented.

The high energy deposition inside the igniter results in the fast expansion of the gas. Figures 13(a)–(i) and 14(a)–(i) show the evolution of the gas pressure and mass density. Strong shock waves are generated from the arc discharge channel, reflected repeatedly by the insulation dielectric walls and finally focused in the center inside the igniter, leading to a

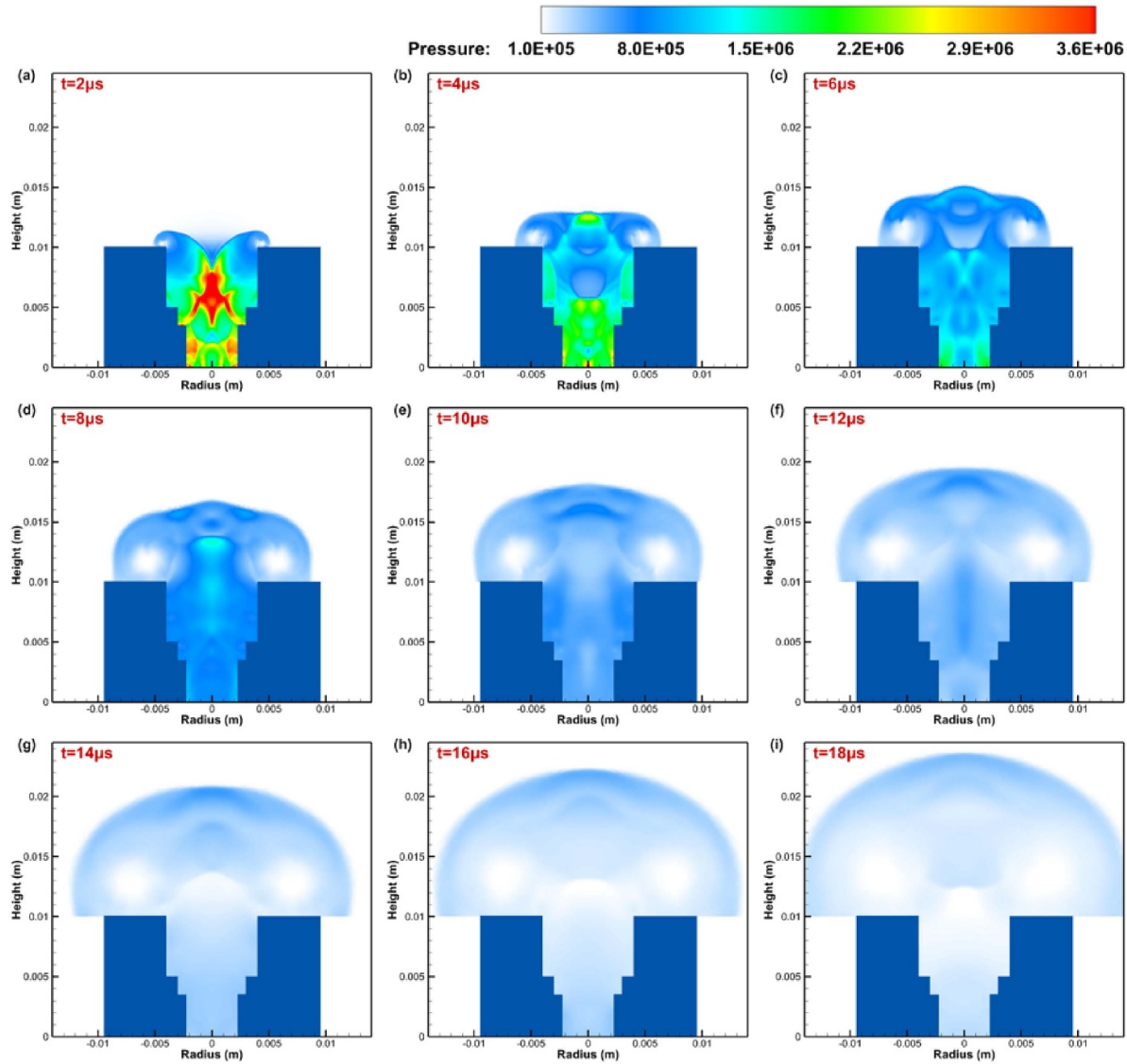


Figure 13. The pressure distribution evolution during the jet stage. The blue represents the igniter. (a) $t = 2 \mu\text{s}$, (b) $t = 4 \mu\text{s}$, (c) $t = 6 \mu\text{s}$, (d) $t = 8 \mu\text{s}$, (e) $t = 10 \mu\text{s}$, (f) $t = 12 \mu\text{s}$, (g) $t = 14 \mu\text{s}$, (h) $t = 16 \mu\text{s}$, (i) $t = 18 \mu\text{s}$, unit: Pa.

region of high pressure (30 bar, figure 13(a)) and high density (4 kg m^{-3} , figure 14(a)). This high-pressure and high-density region is then ‘pushed’ out of the igniter, forming a wavefront propagating with a velocity of $750\text{--}875 \text{ m s}^{-1}$. The pressure of the wave front drops quickly from 20 to 8 bar, the mass density drops from 4 to 2.7 kg m^{-3} over $18 \mu\text{s}$, leaving a low-density region of 0.3 kg m^{-3} after the pressure/mass wave. This low-density region will be filled with new gas when the heated gas is cooled inside the igniter.

The plasma igniter introduces both gas heating effects and chemical effects to the gas mixture. In the presence of combustible mixtures, gas discharges will dissociate the molecules into atoms or radicals. It is interesting to see how the generated active species are distributed and developed in this spark jet igniter. In this section, we take O atoms as a ‘marker’ of active species and study the generation and evolution of the O atoms in the discharge propagation and jet flow stage.

In the discharge propagation stage, the gas temperature remains at a low level (370–600 K, as shown in figure 8), the O atoms are generated mainly through direct electron impact reaction, quenching of excited nitrogen and dissociative recombination [42]. The O atoms are concentrated in the streamer–spark channel with the density of $10^{22}\text{--}10^{23} \text{ m}^{-3}$, as is shown in figures 15(a)–(d). In the discharge propagation stage, the O atoms are generated mainly near the cathode and along the dielectric surface. Once the channel is formed, the O atoms are generated inside the igniter duplicating the distribution of electron density. However, the locally distributed O atoms cannot participate in the following reactions for ignition and combustion.

In the arc discharge stage, the rather high temperature makes the thermal dissociation of oxygen molecules the dominant production mechanism. The spatial–temporal evolution of the O atoms generated in the jet flow stage is shown in figures 16(a)–(i), a rather high density of O atoms ranging from

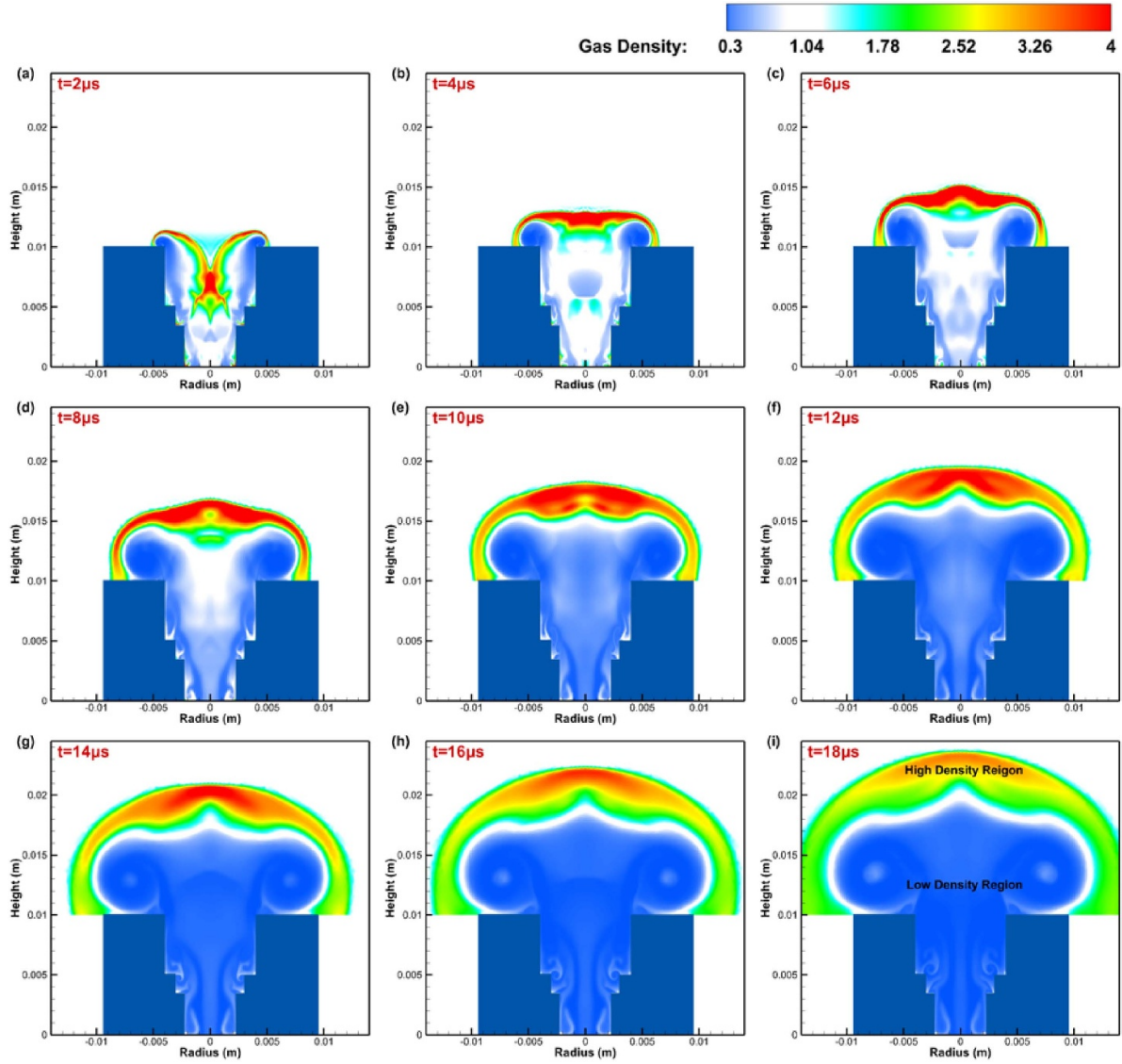


Figure 14. The evolution of gas density during the jet stage, where the blue represents the igniter. (a) $t = 2 \mu\text{s}$, (b) $t = 4 \mu\text{s}$, (c) $t = 6 \mu\text{s}$, (d) $t = 8 \mu\text{s}$, (e) $t = 10 \mu\text{s}$, (f) $t = 12 \mu\text{s}$, (g) $t = 14 \mu\text{s}$, (h) $t = 16 \mu\text{s}$, (i) $t = 18 \mu\text{s}$, unit: kg m^{-3} .

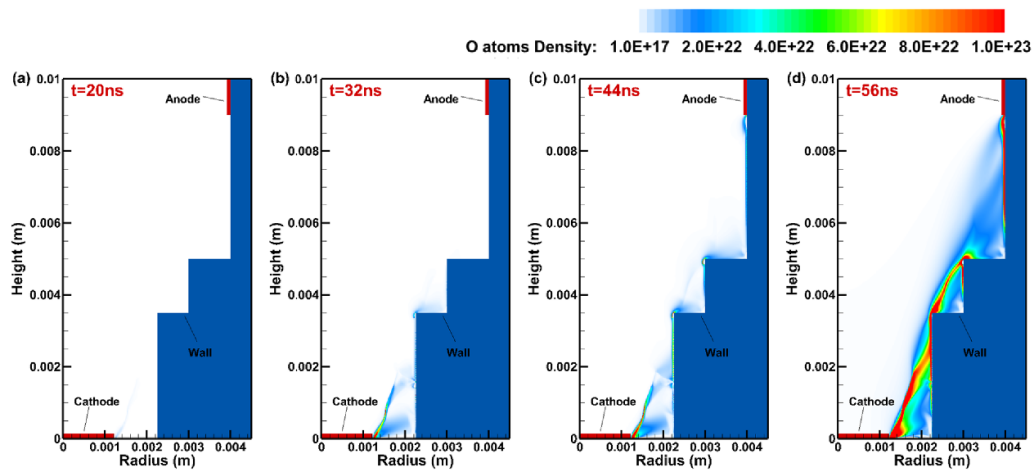


Figure 15. The evolution of O atoms density in steamer discharge during the discharge propagation stage. The red parts represent the cathode and anode and the blue part represents the dielectric wall. (a) $t = 20 \text{ ns}$, (b) $t = 32 \text{ ns}$, (c) $t = 44 \text{ ns}$, (d) $t = 56 \text{ ns}$, unit: m^{-3} .

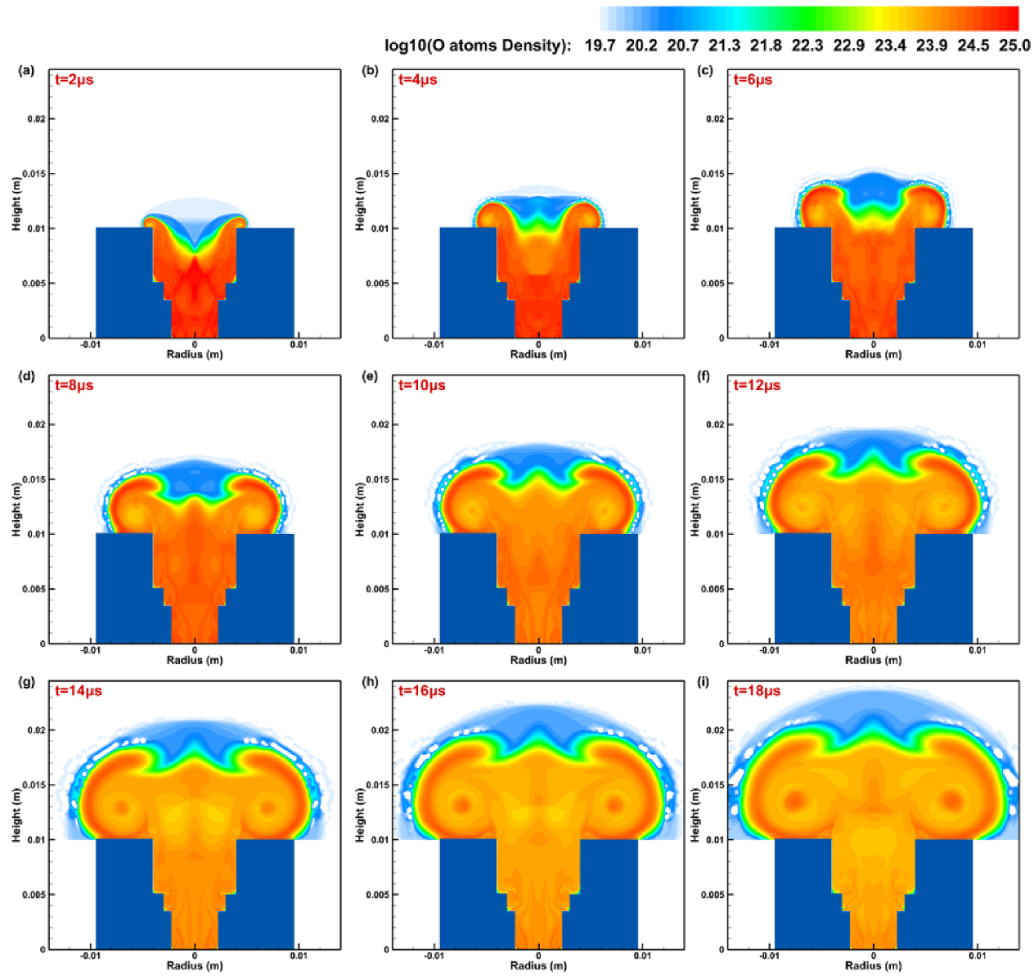


Figure 16. The spatial-temporal evolution of the O atoms number density in the jet flow, (a) $t = 2 \mu\text{s}$, (b) $t = 4 \mu\text{s}$, (c) $t = 6 \mu\text{s}$, (d) $t = 8 \mu\text{s}$, (e) $t = 10 \mu\text{s}$, (f) $t = 12 \mu\text{s}$, (g) $t = 14 \mu\text{s}$, (h) $t = 16 \mu\text{s}$, (i) $t = 18 \mu\text{s}$.

10^{23} m^{-3} and 10^{24} m^{-3} are generated during the expansion of the heated gas. It is interesting to find that the O atoms are mainly generated after the pressure and mass density wave-front.

The line distribution of O atoms and NO molecules are plotted together with the temperature in figure 17. The O atoms and NO molecules are transported out of the cavity with the velocity of $750\text{--}875 \text{ m s}^{-1}$ with an almost constant number density of 10^{24} m^{-3} in the first $20 \mu\text{s}$, indicating that convection is the dominating transport mechanism. The density front and temperature front peaks at the same position, indicating that the generation of the O atoms and NO molecules are caused by the thermal dissociation in the high-temperature region, and note that the high-temperature region is also convection dominating, we can conclude that the transport of active species is affected by both thermal effects and convection.

3.3. The role of the 'ladder-like' geometry in the O atoms evolution of the igniter

The spark jet igniter studied in this work has a unique 'ladder-like' structure inside. In section 3.1 we mentioned that this structure makes it easier for the streamer to attach to the

insulation dielectric, reducing the breakdown voltage and increasing the discharge strength. In this section, we will further discuss the influence of geometry on arc heating and jet flow processes.

To have a comparative view, we repeat the aforementioned calculation with a simplified rectangular geometry as shown in figure 18(a), on the right hand side. With the same energy input, the highest arc temperature in the simplified geometry appears only near the electrodes, and the arc structure is not as clear as that with the 'ladder-like' geometry. The average temperature in the simplified igniter is not affected strongly, ranging from 3000 to 9000 K.

To compare the performance of the igniter with different geometries, we plot the contours of the reaction source term and the flux source term of the O atoms at $18 \mu\text{s}$ in figures 18(b) and (c). At this moment, the jet has developed 2 cm away from the cavity, the density of O atoms decayed in the entire domain in the simplified igniter, while outside the 'ladder-like' igniter, the O atoms density was still increasing chemically in the radial direction.

The O atoms distribution (figure 18(d)) overlaps the distribution of the transport source term. The less heated arc region in the simplified igniter results in weaker transport

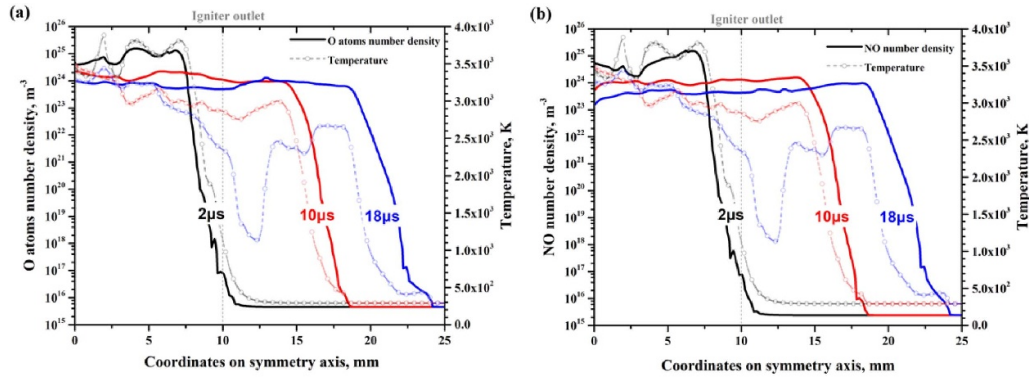


Figure 17. The temperature and species density of the igniter centerline, (a) O atom and (b) NO molecule.

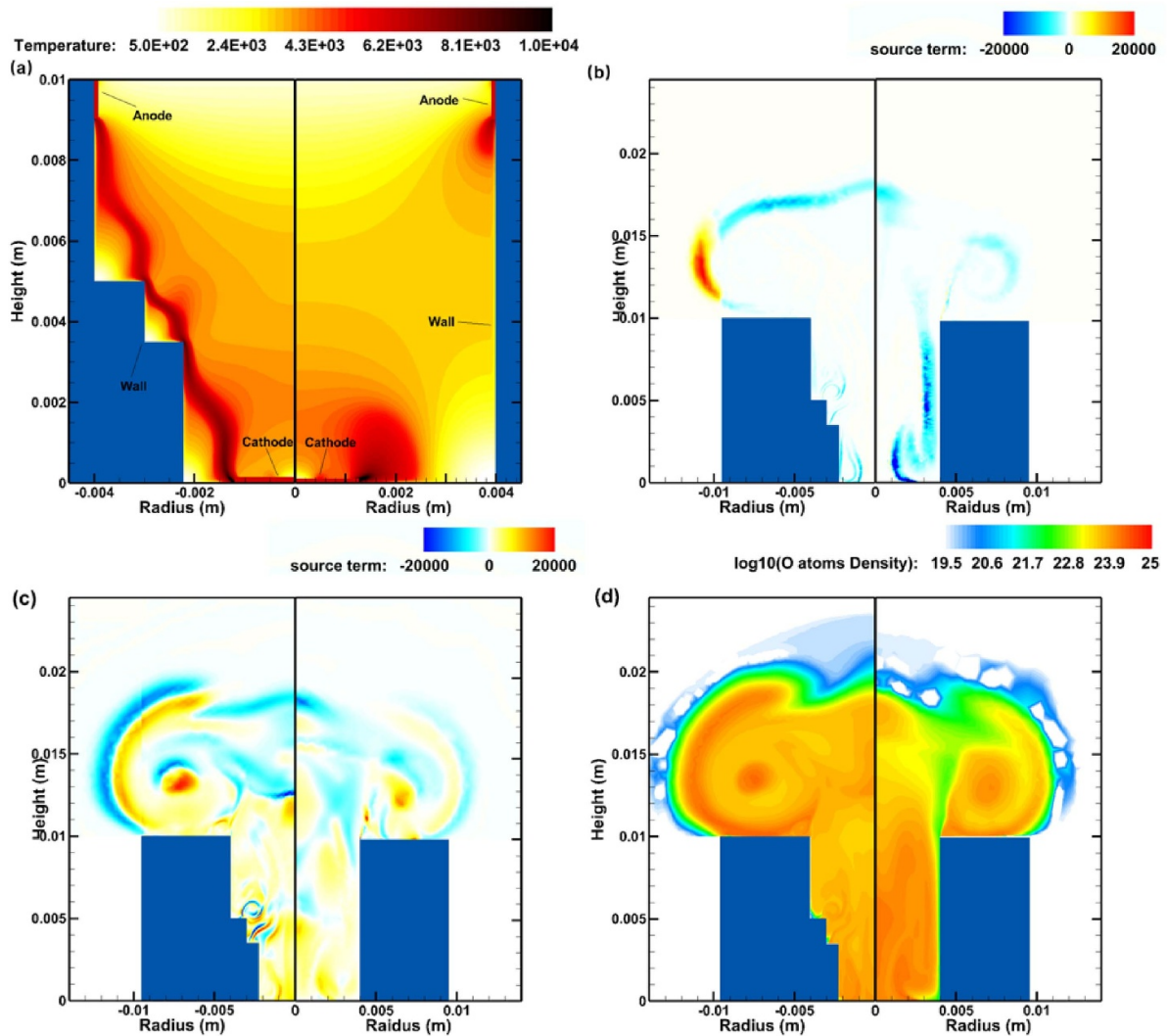


Figure 18. The comparison between the original and modified igniter. (a) The end time temperature distribution in the arc discharge stage (in K). (b) The end time reaction source term of O atoms in the jet stage (in $\text{kg (m}^3 \text{s)}^{-1}$). (c) The end time transport source term of O atoms in the jet stage (in $\text{kg (m}^3 \text{s)}^{-1}$). (d) The end time O atoms density (m^{-3} in logarithm) in the jet flow stage. The left is the original igniter and the right is the igniter with a rectangular structure for comparison.

and vortex structures inside the igniter: the high-temperature region is located mainly inside the igniter instead of being brought out into the ambient gas. The weaker flux and vortex weaken the mixing of activated species with ambient gas. As a result, more active species are left inside the simplified igniter.

4. Conclusion

The plasma-fluid multi-physics process of a spark jet igniter is numerically studied in this work. The *PASSKEY* code (for the nonequilibrium discharge stage) and COMSOL Multiphysics software (for the arc and reactive jet stages) are used together to model the discharge and hydrodynamics characteristics of the spark jet igniter in the static air. The following conclusions are drawn:

- (i) Gas discharge occurs inside the igniter in the form of a streamer starting from the cathode. The existence of the 'ladder-like' dielectric structure promotes the transition from a volumetric streamer to a surface streamer propagating towards the anode within 56 ns. Once a conductive channel is established between electrodes, a new spark channel with an electron density of 10^{21} m^{-3} and an electric field of 100–150 Td is formed.
- (ii) The spark-arc channel is a region of high temperature (up to 7000–10 000 K) caused by energy deposition. The other region inside the spark igniter also reaches as high as 2000–4000 K in tens of microseconds. The high temperature leads to the dissociation of molecules and the expansion of the gases. The heated gas is 'pushed' out of the igniter, forming a 'heating core' with high temperature (2000–3000 K) and high O and NO density (10^{24} m^{-3}) following a wavefront propagating with a velocity of 750–875 m s^{-1} . The calculated evolution of the heating core agrees well with the ICCD measurements in penetration depth (1 cm) and expansion radius (1 cm).
- (iii) The role of the 'ladder-like' structure inside the igniter is studied by comparing it with a simplified rectangular structure igniter. The penetration depth and expansion radius of the heating core are not sensitive to the igniter geometry structure. But the igniter with a 'ladder-like' structure results in higher temperature and active species density in the heating core, as the reflection of the many micro shock waves generated inside the igniter plays a beneficial role in pushing the heated gas and species out of the igniter.

It has to be admitted that the two-dimensional cylindrical model cannot resolve the appearance and characteristics of the arc filaments, thus the predicted peak temperature may differ from observations. The combination of the model of this work with a simplified analytical model focusing on one-arc filaments may be more useful and efficient in the analysis and design of an engineering igniter in the future.

Data availability statement

All data that support the findings of this study are included within the article (and any supplementary files).

Acknowledgments

The work is supported by the National Natural Science Foundation of China (Grant Nos. 51907204, 51790511, 91941105, 91941301, 52025064 and 52007187). The authors are also grateful to the young research group in Atelier des Plasmas for maintenance of the *PASSKEY* code.

ORCID iDs

Xiaochi Ma  <https://orcid.org/0000-0003-0951-9338>
 Yifei Zhu  <https://orcid.org/0000-0001-8989-0051>
 Yun Wu  <https://orcid.org/0000-0002-8575-0665>
 Xiancong Chen  <https://orcid.org/0000-0002-9924-7999>

References

- [1] Ju Y and Sun W 2015 Plasma assisted combustion: dynamics and chemistry *Prog. Energy Combust. Sci.* **48** 21–83
- [2] Do H, Im S-k, Cappelli M A and Mungal M G 2010 Plasma assisted flame ignition of supersonic flows over a flat wall *Combust. Flame* **157** 2298–305
- [3] Wolk B M and Ekoto I 2017 Calorimetry and imaging of plasma produced by a pulsed nanosecond discharge igniter in EGR gases at engine-relevant densities *SAE Int. J. Engines* **10** 970–83
- [4] Topham D, Smy P and Clements R 1975 An investigation of a coaxial spark igniter with emphasis on its practical use *Combust. Flame* **25** 187–95
- [5] Huang S, Zhang Z, Song H, Wu Y and Li Y 2018 A novel way to enhance the spark plasma-assisted ignition for an aero-engine under low pressure *Appl. Sci.* **8** 1533
- [6] Cybyk B, Grossman K and Wilkerson J 2004 Performance characteristics of the sparkjet flow control actuator *2nd AIAA Flow Control Conf.* p 2131
- [7] Cybyk B, Grossman K, Wilkerson J, Chen J and Katz J 2005 Single-pulse performance of the sparkjet flow control actuator *43rd AIAA Aerospace Sciences Meeting and Exhibit* p 401
- [8] Cybyk B, Land H, Simon D, Chen J and Katz J 2006 Experimental characterization of a supersonic flow control actuator *44th AIAA Aerospace Sciences Meeting and Exhibit* p 478
- [9] Zong H-h, Wu Y, Li Y-h, Song H-m, Zhang Z-b and Jia M 2015 Analytic model and frequency characteristics of plasma synthetic jet actuator *Phys. Fluids* **27** 027105
- [10] Zong H-h, Wu Y, Jia M, Song H-m, Liang H, Li Y-h and Zhang Z-b 2015 Influence of geometrical parameters on performance of plasma synthetic jet actuator *J. Phys. D: Appl. Phys.* **49** 025504
- [11] Subramaniam V, Panneerchelvam P and Raja L L 2018 Modeling of thermalization phenomena in coaxial plasma accelerators *J. Phys. D: Appl. Phys.* **51** 215203
- [12] Sary G, Dufour G, Rogier F and Kourtzanidis K 2014 Modeling and parametric study of a plasma synthetic jet for flow control *AIAA J.* **52** 1591–603

- [13] Kourtzanidis K, Dufour G and Rogier F 2020 Self-consistent modeling of a surface ac dielectric barrier discharge actuator: in-depth analysis of positive and negative phases *J. Phys. D: Appl. Phys.* **54** 045203
- [14] Kourtzanidis K and Raja L L 2017 Three-electrode sliding nanosecond dielectric barrier discharge actuator: modeling and physics *AIAA J.* **55** 1393–404
- [15] Nusca M J, McQuaid M J and Anderson W R 2002 Numerical model of the plasma jet generated by an electrothermal-chemical igniter *J. Thermophys. Heat Transfer* **16** 157–60
- [16] Thiele M, Selle S, Riedel U, Warnatz J and Maas U 2000 Numerical simulation of spark ignition including ionization *Proc. Combust. Inst.* **28** 1177–85
- [17] Sharma A, Subramaniam V, Solmaz E and Raja L L 2018 Fully coupled modeling of nanosecond pulsed plasma assisted combustion ignition *J. Phys. D: Appl. Phys.* **52** 095204
- [18] Mao X, Zhong H and Ju Y 2021 2D modeling of plasma-assisted H₂/air ignition in a nanosecond discharge with detailed chemistry *AIAA Scitech 2021 Forum* p 1790
- [19] Zhu Y Parallel streamer solver with kinetics (Available at: www.plasma-tech.net/parser/passkey/)
- [20] Zhu Y, Shcherbanev S, Baron B and Starikovskaia S 2017 Nanosecond surface dielectric barrier discharge in atmospheric pressure air: I. Measurements and 2D modeling of morphology, propagation and hydrodynamic perturbations *Plasma Sources Sci. Technol.* **26** 125004
- [21] Zhu Y, Chen X, Wu Y, Hao J, Ma X, Lu P and Tardiveau P 2021 Simulation of the ionization wave discharges: a direct comparison between the fluid model and E-FISH measurements *Plasma Sources Sci. Technol.* **30** 075025
- [22] Bourdon A, Pasko V, Liu N, Célestin S, Ségur P and Marode E 2007 Efficient models for photoionization produced by non-thermal gas discharges in air based on radiative transfer and the Helmholtz equations *Plasma Sources Sci. Technol.* **16** 656
- [23] Luque A, Ebert U, Montijn C and Hundsdoerfer W 2007 Photoionization in negative streamers: fast computations and two propagation modes *Appl. Phys. Lett.* **90** 081501
- [24] Zhu Y and Starikovskaia S M 2018 Fast gas heating of nanosecond pulsed surface dielectric barrier discharge: spatial distribution and fractional contribution from kinetics *Plasma Sources Sci. Technol.* **27** 124007
- [25] Meek J M 1940 A theory of spark discharge *Phys. Rev.* **57** 722–8
- [26] Popov N 2011 Fast gas heating in a nitrogen–oxygen discharge plasma: I. Kinetic mechanism *J. Phys. D: Appl. Phys.* **44** 285201
- [27] Hagelaar G J M and Pitchford L C 2005 Solving the Boltzmann equation to obtain electron transport coefficients and rate coefficients for fluid models *Plasma Sources Sci. Technol.* **14** 722–33
- [28] Hofmans M, Viegas P, Rooij O V, Klarenaar B, Guaitella O, Bourdon A and Sobota A 2020 Characterization of a kHz atmospheric pressure plasma jet: comparison of discharge propagation parameters in experiments and simulations without target *Plasma Sources Sci. Technol.* **29** 34003
- [29] Viegas P, Hofmans M, van Rooij O, Obrušník A, Klarenaar B L M, Bonaventura Z, Guaitella O, Sobota A and Bourdon A 2020 Interaction of an atmospheric pressure plasma jet with grounded and floating metallic targets: simulations and experiments *Plasma Sources Sci. Technol.* **29** 095011
- [30] Zhu Y, Wu Y, Wei B, Xu H, Liang H, Jia M, Song H and Li Y 2020 Nanosecond-pulsed dielectric barrier discharge-based plasma-assisted anti-icing: modeling and mechanism analysis *J. Phys. D: Appl. Phys.* **53** 145205
- [31] Chen X, Zhu Y and Wu Y 2020 Modeling of streamer-to-spark transitions in the first pulse and the post discharge stage *Plasma Sources Sci. Technol.* **29** 095006
- [32] Naghizadeh-Kashani Y and Gleizes A 2002 Net emission coefficient of air thermal plasmas *J. Phys. D: Appl. Phys.* **35** 2925
- [33] School of Electrical Engineering, Xi'an Jiaotong University Gas discharge plasma database (Available at: www.plasma-data.net)
- [34] Boeuf J and Pitchford L 2005 Electrohydrodynamic force and aerodynamic flow acceleration in surface dielectric barrier discharge *J. Appl. Phys.* **97** 103307
- [35] Rong M, Hong L, Cressault Y, Gleizes A, Wang X, Chen F and Zheng H 2014 Thermophysical properties of SF₆–Cu mixtures at temperatures of 300–30 000 K and pressures of 0.01–1.0 MPa: part 1. Equilibrium compositions and thermodynamic properties considering condensed phases *J. Phys. D: Appl. Phys.* **47** 495202
- [36] Zhong L, Cressault Y and Teulet P 2018 Thermophysical and radiation properties of high-temperature C₄F₈–CO₂ mixtures to replace SF₆ in high-voltage circuit breakers *Phys. Plasmas* **25** 033502
- [37] Taylor R and Krishna R 1993 *Multicomponent Mass Transfer* vol 2 (New York: Wiley)
- [38] Wright M J, Bose D, Palmer G E and Levin E 2005 Recommended collision integrals for transport property computations. Part 1: air species *AIAA J.* **43** 2558–64
- [39] Camac M and Feinberg R M 1967 Formation of NO in shock-heated air *Symp. (Int.) Combust.* **11** 137–45
- [40] Kulikovskiy A 1998 Positive streamer in a weak field in air: a moving avalanche-to-streamer transition *Phys. Rev. E* **57** 7066
- [41] Li X, Sun A, Zhang G and Teunissen J 2020 A computational study of positive streamers interacting with dielectrics *Plasma Sources Sci. Technol.* **29** 065004
- [42] Popov N 2016 Kinetics of plasma-assisted combustion: effect of non-equilibrium excitation on the ignition and oxidation of combustible mixtures *Plasma Sources Sci. Technol.* **25** 043002